

Optomechanical Synchronization across Multi-Octaves Frequency Spans

Caique Rodrigues

University of Campinas

Cauê Kersul

University of Campinas

André Primo

University of Campinas

Michal Lipson

Columbia University <https://orcid.org/0000-0003-2903-3765>

Thiago Alegre

University of Campinas

Gustavo Wiederhecker (✉ gustavo@ifi.unicamp.br)

University of Campinas <https://orcid.org/0000-0002-8216-6797>

Article

Keywords: synchronization, cavity optomechanical devices, optomechanical oscillator, multi-octaves frequency spans

Posted Date: May 4th, 2021

DOI: <https://doi.org/10.21203/rs.3.rs-400062/v1>

License:   This work is licensed under a Creative Commons Attribution 4.0 International License.

[Read Full License](#)

Version of Record: A version of this preprint was published at Nature Communications on September 24th, 2021. See the published version at <https://doi.org/10.1038/s41467-021-25884-x>.

Optomechanical Synchronization across Multi-Octaves Frequency Spans

Caique C. Rodrigues,* Cauê M. Kersul, André G. Primo, Michal Lipson[‡], Thiago P. M. Alegre, and Gustavo S. Wiederhecker[†]

Applied Physics Department, Gleb Wataghin Physics Institute, University of Campinas, Campinas, SP, Brazil

[‡]Department of Electrical Engineering, Columbia University, New York, New York 10027, USA

Experimental exploration of synchronization in scalable oscillator micro systems has unfolded a deeper understanding of networks, collective phenomena, and signal processing. Cavity optomechanical devices have played an important role in this scenario, with the perspective of bridging optical and radio frequencies through nonlinear classical and quantum synchronization concepts. In its simplest form, synchronization occurs when an oscillator is entrained by a signal nearby the oscillator's tone, and becomes increasingly challenging as the frequency detuning increases. Here, we experimentally demonstrate entrainment of a silicon-nitride optomechanical oscillator driven several octaves away from its 32 MHz fundamental frequency. Exploring this effect, we perform a 4:1 frequency division from 128 MHz to 32 MHz. Further developments could harness these effects towards frequency synthesizers, phase-sensitive amplification and nonlinear sensing.

I. INTRODUCTION

Synchronization phenomena lies at the core of time keeping and underpins a vast class of natural phenomena, from life cycles to precision measurements [1]. In a nutshell, synchronization occurs when an oscillatory system has its bare frequency entrained by a weak external signal, which may have a slightly different tempo. Since its observation by Huygens in the 17th century, the synchronization of widely distinct systems have been shown to share remarkably universal features [1, 2], fostering its exploration across many disciplines [3–5]. With the recent convergence among optical, mechanical and electrical waves using scalable microfabrication technologies, synchronization has emerged as a powerful tool targeted not only at technological applications, such as phase-lock loops (PLLs) in radio-based communications [6–8], but also at developing the fundamentals of chaotic systems [9], injection locking [10–12], electro and optomechanical devices [13–20], nonlinear dynamics [21–25], network coupling [26–29], and quantum synchronization [30–35].

Most synchronization realizations occur when the oscillation frequencies involved are barely dissimilar. This is usually the case because most oscillators rely on an underlying frequency-selective resonant response, e.g., mechanical, electrical or optical resonance, which drastically suppresses off-resonant excitations. Despite the weak response to such non-resonant signals, oscillators with a strong nonlinearity may also synchronize when the ratio between external driving frequency (Ω_d) and the oscillation frequency (Ω_0) is close to a rational number $\rho = p/q$ called winding number [36], i.e., the ratio $\Omega_d/\Omega_0 = p/q$ with p, q being coprime integers. Indeed, higher order $p : q$ synchronization features have been experimentally observed in a variety of nonlinear systems,

from Van Der Pol's neon-bulb oscillator [37] to modern spin-torque oscillators [38–40], micro-electro-mechanical systems (MEMS) [41–46], delay-coupled lasers [9, 47], nuclear magnetic resonance laser [48], and on-chip optical parametric oscillators [49]. These higher-order synchronization demonstrations are of major importance in radio-frequency (RF) division applications, which often demand low-power consumption and wide-band operation [50–52].

Within optomechanical devices, high-order synchronization have been overlooked, despite their unique potential for bridging optical and RF signals [53] or enabling role in quantum [32, 54, 55] and classical devices [20, 56]. For instance, the first optomechanical injection-locking demonstration by Hossein-Zadeh et al. [57] showed evidence of synchronization at $\Omega_d = 2\Omega_0$, while Hui Wang et al. [58] demonstrated a Devil's staircase in an on-fiber optomechanical cavity oscillator based on thermal effects. Theoretical work has also suggested weak signatures of higher-order synchronization in optomechanical cavities [59].

Here, we experimentally demonstrate the entrainment of a silicon-nitride optomechanical oscillator (OMO) by an external signal up to four octaves away from its oscillation frequency. Furthermore, the OMO operates in the intriguing regime where higher order synchronization ($p > q$) is actually stronger than the trivial 1 : 1 case, as determined by the degree of nonlinearity set by the laser frequency and intensity. Finally, we explore this regime to experimentally demonstrate a purely optomechanical radio-frequency divider with a phase noise performance better than the 1:1 locking regime. Our results open a route for exploring and engineering nonlinear synchronization in optomechanical oscillators [60], phase-sensitive amplification [61, 62], nonlinear sensing [63], and the collective dynamics of emerging oscillator arrays [29, 64, 65].

* ccr@ifi.unicamp.br

† gsw@unicamp.br

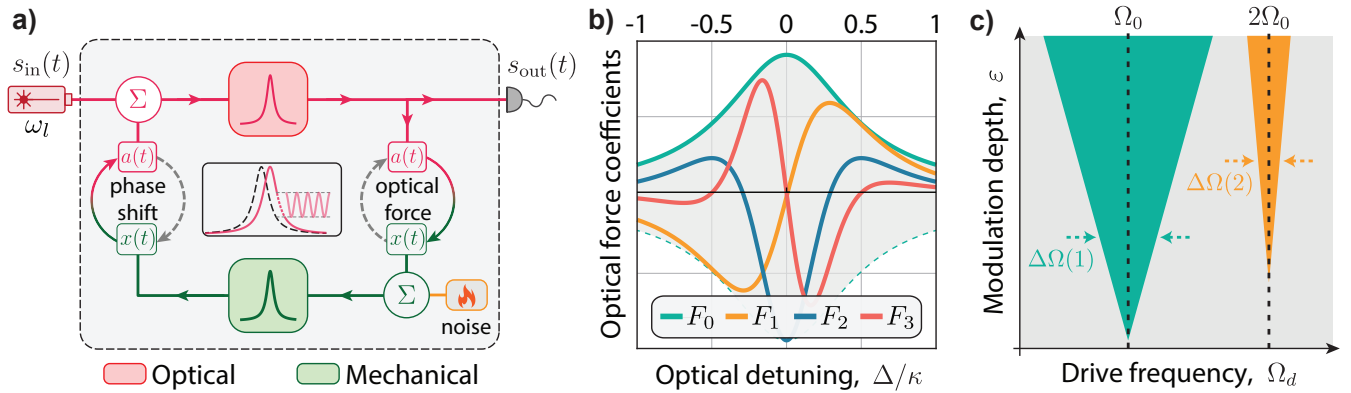


FIG. 1. **High-harmonic response of optomechanical oscillators.** **a)** Optomechanical oscillator feedback diagram. The mechanical degree of freedom, $x(t)$, is initially in equilibrium with the thermal Brownian noise bath, but when a continuous-wave laser excites the optical field within the optical resonator, $a(t)$, the optical phase is imparted by the mechanical motion and transduced – via the optical resonance – to fluctuations on the optical energy. Due to radiation-pressure forces, the mechanical oscillator experiences a feedback (back-action) force that impacts its dynamics; **b)** Optical force components as function of the optical detuning $\Delta = \omega_l - \omega_0$ shown in Eq. (1) (details in the Supplementary Information); **c)** Arnold tongues in the $\varepsilon - \Omega_d$ space illustrating 1 : 1 and 2 : 1 entrainment.

II. RESULTS

A. Synchronization Background

The general structure of optomechanical oscillators dynamic can be represented by the feedback diagram shown in Fig. 1(a). The optical force driving the mechanical mode depends nonlinearly on the displacement, $x(t)$. Thus, the Lorentzian-shape of the optical resonance provides a unique route to tailor the degree of nonlinearity of the optical force, defining how different harmonics of the mechanical oscillation are excited during the optical-to-mechanical transduction.

To establish synchronization, we apply a weak intensity modulation to the optical driving power, $P_{in}(t) = P_0 [1 + \varepsilon \sin(\Omega_d t)]$, where P_0 is the continuous-wave average power and $\varepsilon \ll 1$ is the modulation depth. In the unresolved sideband regime, where Ω_0 is smaller than the optical linewidth κ , the essence of the feedback loop of Fig. 1(a) is captured by introducing a delayed mechanical response $x(t) \rightarrow \tilde{x}(t - \tau)$, where \tilde{x} is a normalized dimensionless displacement (details in the Supplementary Information). The optical force can then be efficiently written as a power series in $\tilde{x}(t - \tau)$,

$$F_{opt}(t) = f_{opt} [1 + \varepsilon \sin(\Omega_d t)] \sum_{n=0}^{\infty} F_n \tilde{x}^n(t - \tau), \quad (1)$$

whose strength depends not only on the overall optical force strength, f_{opt} , but also on the dimensionless coefficients F_n , which dictates the intensity of the nonlinearity and their detuning dependence, as shown in Fig. 1(b). Important optomechanical properties, such as optical cooling/amplification or spring effect [54, 66], are described by considering up to the first-order term F_1 in Eq. (1). The modulation depth dependent terms

($\propto \varepsilon$) enable the injection-locking and synchronization of the OMO to an external drive. While F_0 and F_1 hardly provide new insights into synchronization properties, the quadratic and cubic terms (F_2 and F_3) highlight a key aspect explored in this work: nonlinear synchronization properties can be adjusted with an easily accessible parameter, the optical detuning, which significantly changes their relative strengths, as shown in Fig. 1(b).

The impact of these nonlinearities in the synchronization dynamics can be cast into the well-known Adler’s model, which describes the slowly varying phase dynamics of an oscillator perturbed by a weak external drive [59, 67]. Indeed, we show in “Methods” that the Taylor-series description of Eq. (1) leads to an effective Adler model when the optical modulation frequency is tuned towards a chosen harmonic of the mechanical frequency [1]. Synchronization in this model arises when the perturbation strength overcomes the frequency mismatch between the drive and oscillator’s harmonics. As the external drive frequency Ω_d is swept around the oscillator harmonics, the synchronization condition may still be satisfied and defines a region in a $\varepsilon - \Omega_d$ space known as Arnold tongues (ATs) [1], illustrated in Fig. 1(c). Such response to higher harmonics could be readily explored for radio-frequency division, as we demonstrate later.

B. Experimental Results

To experimentally assess high-order synchronization and measure the ATs, it is important to harness the nonlinear response of an OMO. We achieve this control by employing a dual-disk optomechanical cavity based on silicon-nitride [68, 69], as shown schematically in Fig. 2(a). This cavity supports a relatively low frequency ($\Omega_m/2\pi = 31.86$ MHz) and high quality factor

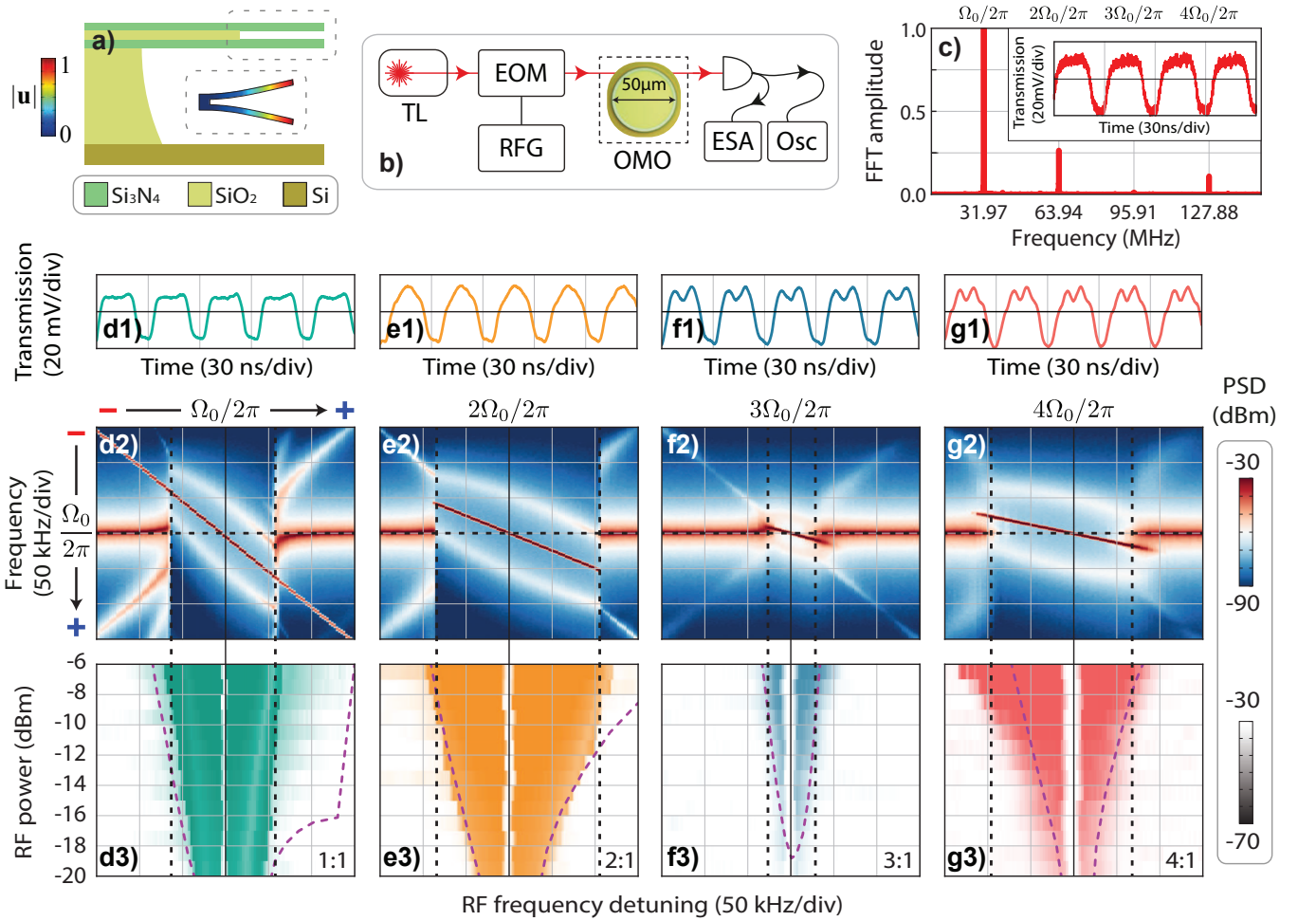


FIG. 2. **Experimental demonstration of multi-octave synchronization.** **a)** Illustration of the silicon nitride dual-disk optomechanical cavity used in the experiment. The inset shows the simulated flapping mechanical mode displacement profile $|u|$; **b)** Schematic of the experimental setup used; TL is the tunable laser source; EOM: electro-optic modulator; RFG: radio-frequency generator; ESA: electrical spectrum analyzer; Osc: oscilloscope; **c)** Magnitude of the fast-Fourier transform of the OMO output signal (inset); **d1-g1)** Time-trace of the OMO output entrained at $p = 1$ (**d1**) until $p = 4$ (at **g1**). A RF injection power of -10 dBm ($\varepsilon \approx 4\%$) was used; **d2-g2)** RF spectrograms measured as the injection signal frequency is swept from lower to higher frequencies around each OMO harmonic, $p = 1$ (**d2**) until $p = 4$ (at **g2**), for an injection RF power of -10 dBm. The vertical RF frequency axis is always centered at the mechanical oscillation frequency $\Omega_0/2\pi$ and increases from top to bottom, as the symbols minus and plus suggests. The same is true for the horizontal axis, which increases from the left to the right; **d3-g3)** Measured Arnold tongues corresponding to each harmonic, obtained by stacking horizontal linecuts along the dashed black line in data shown in **d2-g2**). The purple curves are the simulated ATs and the colorscale of each plot matches the grayscale range shown in the right.

mechanical mode ($Q_m = 1250$) [70], which is coupled to a transverse-electric optical mode ($Q_{\text{opt}} = 1.6 \times 10^5$ at a wavelength $\lambda \approx 1556$ nm) with an optomechanical coupling rate $g_0/2\pi = 16.2$ kHz. The experimental setup, shown in Fig. 2(b), essentially consists of an intensity-modulated external cavity tunable laser that is coupled to the optomechanical cavity using a tapered fiber [68]. The output light is analyzed with an oscilloscope and an electrical spectrum analyzer (ESA) that reveals the dynamics of the oscillator while monitoring the optical transmission.

To transition this optomechanical cavity into an OMO

we raise the pump power to $P_0 = 480 \mu\text{W}$ and fine-tune its wavelength such that the detuning between the laser frequency and the cavity resonance corresponds to $\Delta = 0.35\kappa$ ($\Delta/2\pi \approx 408$ MHz), which is inferred by monitoring the optical transmission. A typical OMO free-running output signal and the corresponding Fourier transform are shown in Fig. 2(c), revealing the mildly nonlinear characteristic with a few noticeable harmonics. Interestingly, at this detuning, both the F_0 and F_1 terms in Eq. (1) are of similar strength (see Fig. 1(b)), suggesting that the nonlinear response to an injection signal should be readily observed. To observe injection-locking,

the laser intensity modulation is activated and the modulation frequency is swept around the OMO fundamental frequency and its harmonics ($p = 1 - 4$ and $q = 1$). The time-traces in Fig. 2(d1-g1) are captured with the injection signal frequency being precisely matched to each harmonic using a RF power of -10 dBm. As the RF driving frequency is detuned from each harmonic, the OMO response is monitored through the RF spectrum centered around the fundamental frequency Ω_0 , as shown in the density plots of Fig. 2(d2-g2). At the left-hand side of these plots, the RF tone is far away from the OMO harmonics and do not synchronize, thus, both oscillator and drive frequencies appear as distinct peaks, accompanied by nonlinear mixing products typical of driven oscillators [41]. When the RF tone approaches a harmonic, a clear transition occurs and a single RF peak emerges, which is one major signature of synchronization. The first striking feature is the observation of strong synchronization for all the driving harmonics, a phenomenon that has not been reported in optomechanical systems. Second, and most important, the width of the synchronization region for $p = 2, 4$ is larger than the fundamental harmonic ($p = 1$). It is also remarkable that the $p = 3$ synchronization window is relatively small, counterposing the hierarchy among harmonics.

To map the synchronization window into Arnold tongues and understand the role played by the optical modulation depth, we performed the measurements shown in Fig. 2(d2-g2) for a range of RF powers, and built the ATs shown in Fig. 2(d3-g3). The colored regions indicate a synchronized state, and were obtained by stacking RF spectral slices along the OMO frequency, given by the horizontal dashed-lines in Fig. 2(d2-g2). It is worth pointing out that the highest RF power (-6 dBm) corresponds to a modulation depth $\varepsilon \approx 6\%$, ensuring a weak perturbation regime. Although the existence of higher order tongues could be anticipated by qualitative analysis of the nonlinear terms in Eq. (1), further theoretical analysis is necessary to precisely picture their nature.

C. Discussion

In order to study the observed AT behavior, we perform numerical simulations of the exact coupled equations describing the mechanical and optical mode's dynamics, and the simulated Arnold tongues are shown in Fig. 3(a). Despite the specific parameters that influence the precise behavior of the optomechanical limit cycles[59], such as optical detuning, optomechanical coupling, and optical/mechanical linewidths, a good agreement is observed between the measured and simulated tongues. Such agreement suggests that the observed features are indeed dominated by the optomechanical interaction itself, in contrast to silicon optomechanical devices where thermal and charge carriers effects strongly influences the self-sustaining oscillator dynamics [19, 71]. Although the numerical model is useful for confirming the

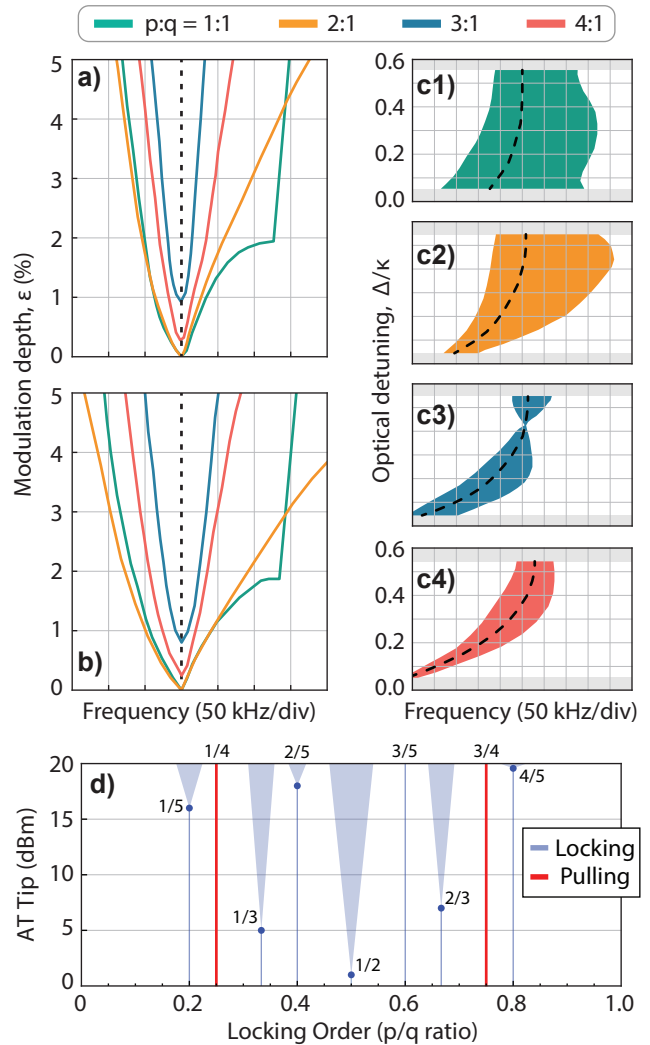


FIG. 3. **Numerical analysis and experimental observation of fractional synchronization.** **a)** Arnold tongues boundaries simulated using the complete coupled optomechanical equations. The horizontal scale is the same used in experimental data of Fig. 2(d3-g3), revealing a good agreement; **b)** Same simulation done as **a)** but now considering only one parametric term in each simulation, i.e., the green (1 : 1) boundary was simulated considering $\varepsilon F_1 = \varepsilon F_2 = \varepsilon F_3 = 0$ but $\varepsilon F_0 \neq 0$ (details in the Supplementary Information). The yellow (2 : 1) boundary has only the term $\varepsilon F_1 \neq 0$, the blue (3 : 1) has $\varepsilon F_2 \neq 0$ and the red (4 : 1) has $\varepsilon F_3 \neq 0$; **c1)-c4)** Impact of optical detuning Δ in the ATs, showing their tunability and the possibility of a vanishing $p = 3$ tongue at $\Delta \approx 0.43\kappa$ for the parameters used. These maps were simulated using $\varepsilon = 5\%$ and the black-dashed line is the mechanical oscillation frequency, which increases with Δ because of the optical spring effect; **d)** Measured fractional synchronization threshold to observe a finite-width AT. The red-lines indicate the locking orders that did not synchronize and only frequency pulling was observed. The Arnold tongues shown are illustrations (see Supplementary Information for actual data).

optomechanical nature of the observed effects, it hardly

provides any analytical insight on the origins of the observed synchronization effects. 275 our semi-analytical approximations ($\varepsilon \approx 100\%$).

We obtain further insight by approximating the optical force as delayed power series, as suggested in Eq. (1). 220 This analysis allows exploring the synchronization role of each nonlinear component F_n in Eq. (1) and elucidates the underlying structure of high-harmonic synchronization. The nonlinear components that *are not* proportional to the driving signal define a “forced Van der Pol-Duffing oscillator” responsible for the oscillator limit cycle observed in Fig. 2(c). 225

The synchronization dynamics is related to the terms proportional to the RF driving signal ($\propto \varepsilon$). However, in addition to the usual non-parametric excitation ($\propto \varepsilon F_0$), 230 the injection signal contribute to time-dependent coefficients in the mechanical oscillator dynamical equation. Physically, these time-varying coefficients indicate that the external signal modulates the oscillator’s frequency and damping properties, leading to linear ($\propto \varepsilon F_1$) and nonlinear ($\propto \varepsilon F_{2,3}$) parametric resonance effects, a situation resembling the dynamics of a nonlinear Mathieu equation [69, 72]. 235

By neglecting all but one time-dependent term in the numerical simulations, we could identify how each harmonic ($p = 1 - 4$) is related to the force expansion coefficients shown in Fig. 1(b). The resulting map is shown in Fig. 3(b), where each boundary was simulated considering only one parametric term, while all the others were set to zero. The resemblance with the full model simulation at Fig. 3(a) is remarkable. This analysis reveals that the terms εF_{p-1} in the force expansion is the leading contribution to the $p : 1$ AT, for all measured harmonics. For instance, as the $p = 3$ entrainment occurs due to the εF_2 parametric term, the thinner tongue observed in Fig. 2(f3) is explained by the negligible value for F_2 at this detuning. Interestingly, although quadratic force terms like $F_2 x^2$ are often ignored in nonlinear mechanical oscillators (as they arise from an asymmetric elastic potential energy), here, they emerge naturally from the Lorentzian shape of the optical mode and can be tuned with the optical detuning. 240 245 250 255

The insights brought by our semi-analytical model suggest that tunable Arnold tongues should be feasible. In Fig. 3(c1-c4) we show a full numerical simulation of the ATs as a function the optical detuning, confirming this possibility. In particular, a complete suppression of $p = 3$ tongue is attainable (Fig. 3(c3)). Such rich response to higher harmonic excitation led us to verify whether our OMO could also respond to fractional frequency excitation, i.e., where p/q is not an integer number. These experimental results are summarized in Fig. 3(d) but the full map can be found in the Supplementary Information for various subharmonics of the mechanical frequency, revealing terms of the famous Farey sequence known in number theory [36]. Note, however, that the injection signal power required to observe fractional tongues were substantially larger, with some fractions (e.g., 4/5) requiring a full modulation, which is beyond the reach of 260 265 270 275

D. Phase Noise & Frequency Division

An important aspect often praised when investigating synchronization and injection-locking phenomena is the reduction of phase noise (PN) in free-running oscillators. While optomechanical oscillator’s phase noise (PN) has been previously explored [15, 57, 65, 71, 73], its characteristics under high harmonic injection are not known. In Fig. 4(a) we show the measured PN at the fundamental oscillator frequency for the free-running OMO and injection-locked at the harmonics $p = 1 - 4$ (see “Methods” for details). The PN curves were taken using a constant RF power of -10 dBm ($\varepsilon \approx 4\%$) for all harmonics. The general behavior of the free-running OMO PN has been discussed previously [73] and it is influenced by various noise sources, such as flicker, thermomechanical, amplitude-to-phase conversion, and others [74]. When injection locked at $p = 1$ (green curve), the PN performance improves significantly, and the PN of the higher harmonics is surprisingly low, despite that the same modulation depth was employed. Indeed, the $p = 2$ injection offers an improvement over the trivial $p = 1$ case, $p = 3$ is slightly deteriorated, and $p = 4$ PN suffers significant penalty. 280 285 290 295 300

To investigate the RF power dependence of each harmonic, PN curves were measured over a range of RF powers and the integrated phase-noise curves (from 100 Hz to 10 kHz) are shown in Fig. 4(b). These confirm the superior PN performance of $p = 2$, but also evidences that higher harmonics need an extra RF power to overcome the $p = 2$ PN, noticeable along the horizontal dashed line in Fig. 4(b). A qualitative understanding of the observed PN behavior can be cast upon previous investigations in the context of superharmonic injection-locking [7, 75–77]. When the injection-signal PN is negligible, the phase-noise of a super-harmonic injected oscillator is written as 305 310 315

$$\mathcal{L}(\Omega) = \frac{\mathcal{L}_{\text{free}}(\Omega)}{1 + (\Delta\Omega_n/\Omega)^2 \cos^2 \theta}, \quad (2)$$

where $\mathcal{L}_{\text{free}}(\Omega)$ is the free-running OMO PN spectra; $\Delta\Omega_n$ is the locking range (AT width) for each harmonic; θ is the phase offset between the injection signal and the OMO. Apart from the phase offset θ , the AT width determines the locking range and is often associated with good phase noise performance. Indeed, the wider lock ranges $\Delta\Omega_2$ observed for the 2:1 injection are associated with a better PN across the whole injection range of Fig. 4(b). For the 3:1 and 4:1 PNs cases, however, the trend is not as clear. While the phase-noise is reduced as the lock-range increases, the 4:1 PN curve in Fig. 4(b) is lagging the 3:1 injection by almost 6 dB, despite the wider 4:1 tongue. Although it is not clear all the factors contributing to this discrepancy, we verified in numerical simulations that the phase-offset θ varies among harmonics and 320 325

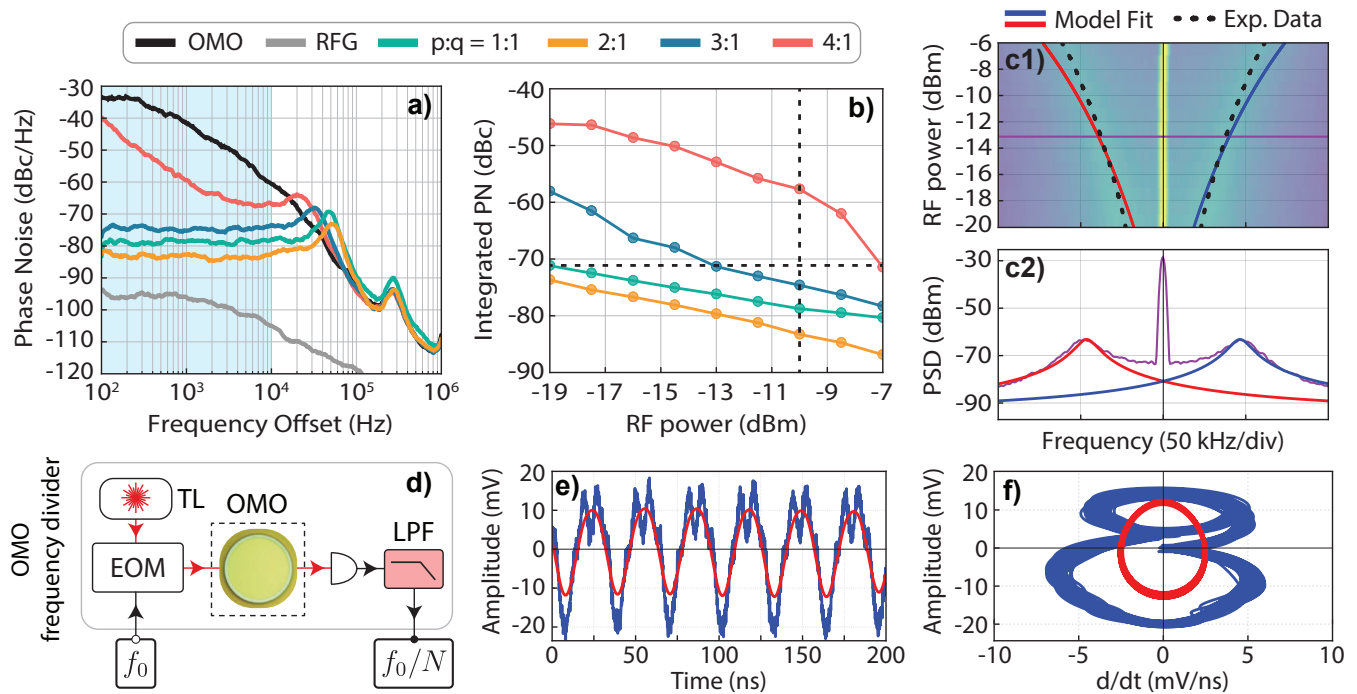


FIG. 4. **Phase-noise reduction and frequency division operation.** **a)** Measured one-sided phase noise spectral density for the free-running (black), injection-locked (colored) and RF injection signal (gray); **b)** Integrated phase noise (from 100 Hz to 10 kHz, which is the light blue region of **a**) for the injection locked OMO; color-code is show in top bar; **c1)** Comparison between experimental data sidebands and the semi-analytical model. The colormap is the experimental PSD centered at $\Omega_0/2\pi$ showing the sidebands for reference; **c2)** Experimental power spectral density (PSD) in purple for a RF power of -13 dBm, which is the same horizontal purple linecut at **c1)**, showing the agreement between semi-analytical model and experimental data for these sidebands, for both frequency and linewidth; **d)** Schematic of the optomechanical frequency divider; **e)** Optomechanical frequency division showing the raw and low-pass filtered OMO output under (4 : 1) injection with -10 dBm RF power; **f)** Phase-space plot of the time-domain signals shown in **e**).

could partially contribute to the observed mismatch. One unique factor contributing to these phase offsets in non-linear oscillators is the strong frequency pulling [78, 79] that distinctively shifts the bare OMO frequency for each harmonic. Indeed, we can notice in the injection maps of Fig. 2(d2-g2) that the locking frequency loci are not symmetric relative to the OMO frequency. For example, Fig. 2(g3) is shifted towards lower frequencies, while Fig. 2(e3) shifts toward higher frequencies. Such shifts are also anticipated by our semi-analytical model, and can be traced back to the effective perturbation strength and frequency mismatch in the Adler’s model (see “Methods”). These nonlinearities also highlight the weakness of neglecting the amplitude-phase coupling in the PN modelling of OMOs.

Another feature that supports the amplitude-phase coupling effects in the PN spectrym, which is not readily captured by the simple model leading to Eq. (2), is the presence of the sidebands appearing in Fig. 4(a) between 20 kHz and 60 kHz. In contrast to the fixed-frequency satellite peaks at 150 kHz, which are caused by parametric mixing with a spurious mechanical mode, these peaks are intrinsic to the nonlinear locking dynamics of OMOs. These sidebands were first discussed by Bagheri et al. [20]

and attributed to coupling between phase and amplitude dynamics that are intrinsic to OMOs. Based upon our amplitude-phase analytical model leading to the effective Adler equations (Eq. (4)), we derive a quantitative model, in similarity to spin-torque oscillators [39], which predicts both frequency splitting and linewidth of these sidebands. Despite the various approximations necessary to reach this analytical amplitude-phase model, the fitted model agrees remarkably well with the experimental data, as shown in Fig. 4(c1) and Fig. 4(c2).

In the context of higher-order synchronization, the demonstrated phase-noise performance could be explored towards superharmonic frequency dividers [7, 8], which generate RF signals at a fraction of a higher frequency reference. Despite their lower power-consumption advantages over other frequency dividers, such as regenerative and parametric dividers [8], they usually suffer from a limited locking range. An experimental schematic that could realize such divider is illustrated in Fig. 4(d), where a low-pass RF filter rejects the higher-harmonics generated by the OMO and delivers an output signal at a fraction of the injected reference, f_0/N . As a proof-of-principle, we emulate this device by numerically performing the low-pass-filter (3rd order Butterworth filter) op-

eration on the experimental data corresponding to -10 dBm in Fig. 4(b). The time-traces before and after the filtering operation are shown in Fig. 4(e), while Fig. 4(f) shows a “phase-space” plot spanning 1 μ s (\approx 30 periods) with the horizontal axis as the derivative of the signals. These results show that OMO-based frequency dividers could be readily derived from the higher-order synchronization reported in this work and benefit from the broad locking range observed for the even harmonics.

CONCLUSIONS

We have experimentally demonstrated an optomechanical oscillator entrained by high-order harmonics that can enable purely optomechanical frequency division. The wider locking range observed for the higher harmonics, and its theoretical mapping to each nonlinear term in the oscillator dynamics, open new routes to control nonlinear synchronization phenomena in optomechanical oscillators, including the tailoring of the nonlinear response through the laser-cavity detuning and also frequency synthesizers optomechanical devices. Furthermore, the importance of nonlinear parametric effects could also significantly impact phase-sensitive amplification [80] and nonlinear sensing [63] with optomechanical devices. The demonstrated entrainment should also enable novel configurations for coupling and controlling optomechanical arrays based on dissimilar resonators. The demonstration of locking at fractional harmonics could also be a starting point for further nonlinear dynamics investigations within an optomechanical platform.

III. METHODS

a. Optical energy. The optical energy dependence on the laser-cavity detuning and mechanical displacement is given by,

$$|a|^2 = \frac{\kappa_e}{(\Delta - Gx)^2 + \kappa^2/4} P_{\text{in}}, \quad (3)$$

in which two key parameters that will enable the tuning of the OMO nonlinear response arise, the input laser power, P_{in} , and the detuning, $\Delta = \omega_l - \omega_0$, between the pump laser (ω_l) and optical mode (ω_0) frequencies; x is the mechanical mode amplitude, $G = \partial\omega/\partial x$ is the optomechanical pulling-parameter, κ is the optical mode linewidth and κ_e is the external coupling to the bus waveguide [3].

b. Effective Adler model. By employing the Krylov-Bogoliubov-Mitropolsky (KBM) time-averaging method [81] at the mechanical oscillator equation, an effective Adler’s equation may be derived (details in the Supplementary Information),

$$\dot{\Phi} = \nu(\rho) + \varepsilon \frac{\Delta\Omega(\rho)}{2} \sin(\rho\Phi). \quad (4)$$

where Φ is the mechanical oscillator phase correction and $\dot{\Phi}$ denote its time derivative; $\nu(\rho)$ is the mean correction of Ω_0 and $\Delta\Omega(\rho)$ is the size of the synchronization window at a particular harmonic $\rho = p/q$. Although many approximations must be carried on, this analysis relates the Taylor series coefficients in Eq. (1) with the coefficients $\nu(\rho)$ and $\Delta\Omega(\rho)$ in the effective Adler’s model Eq. (4), providing a quantitative description of the width hierarchy among the measured ATs.

c. Experimental setup. A full schematic of the experimental setup is shown in the Supplementary Information, along with optical and mechanical characterization of the bare resonator data. The optical transmission and the RF spectral measurements for the bare resonator properties were taken at low pump powers ($< 50 \mu$ W). The laser wavelength and detuning is accurately monitored using a Mach-Zehnder Interferometer (MZI) and a HCN gas cell. The cavity is inside a vacuum chamber with pressure of ≈ 0.1 mbar and at room temperature. Finally, the transduced signal goes to two detectors: a power meter (PM) that will track the optical mode and a fast detector (NewFocus 1617AC Balanced Photodetector) with 800-MHz bandwidth whose electrical output feeds both the electric-spectrum analyser (ESA, Keysight N9030) and oscilloscope (OSC, DSO9254A). There was also a feedback loop between the PM and the TL to lock the signal, preventing the optical resonance to drift due to unwanted external perturbations.

d. Phase noise. To derive the approximate expression for the phase noise (Eq. (2)), we must start from the general PN expression [7, 75],

$$\mathcal{L}(\Omega) = \frac{(\Delta\Omega_n/n)^2 \mathcal{L}_{\text{inj}}(\Omega) \cos^2 \theta + \Omega^2 \mathcal{L}_{\text{free}}(\Omega)}{\Delta\Omega_n^2 \cos^2 \theta + \Omega^2}. \quad (5)$$

Since the injection-locking signal is derived from a stable RF frequency source (Agilent PSG E8251), $\mathcal{L}_{\text{inj}}(\Omega)$, the injection signal PN spectra, is order of magnitude smaller than $\mathcal{L}_{\text{free}}(\Omega)$, and then $\mathcal{L}_{\text{inj}}(\Omega)/\mathcal{L}_{\text{free}}(\Omega) \rightarrow 0$ results in Eq. (2). The modulation depth as function of the RF power is given by $\varepsilon = \pi\sqrt{P_{\text{RF}}R}/V_\pi$, where $R = 50 \Omega$ and $V_\pi = 5.5$ V is the optical modulator parameter. The phase-angle is given by $\theta = \arcsin[(\Omega_0 - \Omega_d/n)/\Delta\Omega_n]$.

e. Simulations. The acquired data was compared with numerical simulations using Julia language together with well known and powerful packages like ODE.jl and DifferentialEquations.jl. As we are dealing with a stiff system, i.e., there is more than one natural time scale for this system and they differ by many order of magnitudes, analysing the system using methods like Euler or Runge-Kutta would be too much expensive, requiring us a time-step too small, making simulations impossible due to hardware limitations. Nevertheless, we simulate the system for many modulation depths ε while the RF signal sweeps around some chosen $p : q$ region, revealing the nature of synchronization. With the obtained time trace, we then locally Fourier transformed the data to constructed the spectrogram, where we finally obtained

all the datas shown in this article. A detailed discussion about the numerical simulation is available at the Supplementary Information. The mechanical mode effective mass and the zero point fluctuation were obtained from COMSOL Multyphysics finite element simulations, $m_{\text{eff}} = 101.82$ pg, $x_{\text{zpf}} = 1.536$ fm, leading to an optomechanical pulling parameters $G/2\pi = (g_0/2\pi)/x_{\text{zpf}} = 10.546$ GHz/nm.

ACKNOWLEDGEMENT

This work was supported by São Paulo Research Foundation (FAPESP) through grants 2019/14377-7,

-
- [1] A. Pikovsky, M. Rosenblum, J. Kurths, and R. C. Hilborn, Synchronization: A Universal Concept in Non-linear Science, *American Journal of Physics* **70**, 655 (2002).
- [2] A. Jenkins, Self-oscillation, *Physics Reports* **525**, 167 (2013).
- [3] M. Aspelmeyer, T. J. Kippenberg, and F. Marquardt, Cavity optomechanics, *Reviews of Modern Physics* **86**, 1391 (2014).
- [4] S. Strogatz, M. Friedman, A. J. Mallinckrodt, and S. McKay, *Nonlinear Dynamics and Chaos: With Applications to Physics, Biology, Chemistry, and Engineering*, *Computers in Physics* 10.1063/1.4823332 (1994).
- [5] E. A. Jackson and R. W. Rollins, *Perspectives of Non-linear Dynamics*, Vol. 1, *American Journal of Physics* 10.1119/1.16510 (1991).
- [6] B. Razavi, A study of injection locking and pulling in oscillators, in *IEEE Journal of Solid-State Circuits*, Vol. 39 (2004) pp. 1415–1424.
- [7] F. Plessas, A study of superharmonic injection locking in multiband frequency dividers, *International Journal of Circuit Theory and Applications* **39**, 397 (2011).
- [8] H. R. Rategh and T. H. Lee, Superharmonic injection-locked frequency dividers, in *Phase-Locking in High-Performance Systems: From Devices to Architectures* (IEEE JOURNAL OF SOLID-STATE CIRCUITS, 2003).
- [9] W. A. S. Barbosa, E. J. Rosero, J. R. Tredicce, and J. R. Rios Leite, Statistics of chaos in a bursting laser, *Physical Review A* **99**, 053828 (2019).
- [10] M. Shi, L. Yi, and W. Hu, High-Resolution Brillouin Optoelectronic Oscillator Using High-Order Sideband Injection-Locking, *IEEE Photonics Technology Letters* **31**, 513 (2019).
- [11] D. Marković, J. Pillet, E. Flurin, N. Roch, and B. Huard, Injection Locking and Parametric Locking in a Superconducting Circuit, *Physical Review Applied* **12**, 024034 (2019).
- [12] G. Arregui, M. F. Colombano, J. Maire, A. Pitanti, N. E. Capuj, A. Griol, A. Martínez, C. M. Sotomayor-Torres, and D. Navarro-Urrios, Injection locking in an optomechanical coherent phonon source, *Nanophotonics* **10**, 1319 (2021).
- [13] I. Mahboob, K. Nishiguchi, H. Okamoto, and H. Yamaguchi, Phonon-cavity electromechanics, *Nature Physics* **8**, 387 (2012).
- [14] K. Huang and M. Hossein-Zadeh, Injection locking of optomechanical oscillators via acoustic waves, *Optics Express* **26**, 8275 (2018).
- [15] C. Bekker, R. Kalra, C. Baker, and W. P. Bowen, Injection locking of an electro-optomechanical device (2017).
- [16] J. G. Huang, Y. Li, L. K. Chin, H. Cai, Y. D. Gu, M. F. Karim, J. H. Wu, T. N. Chen, Z. C. Yang, Y. L. Hao, C. W. Qiu, and A. Q. Liu, A dissipative self-sustained optomechanical resonator on a silicon chip, *Applied Physics Letters* **112**, 051104 (2018).
- [17] J. Sheng, X. Wei, C. Yang, and H. Wu, Self-Organized Synchronization of Phonon Lasers, *Physical Review Letters* **124**, 53604 (2020).
- [18] D. Xu, Z.-Z. Han, Y.-K. Lu, Q. Gong, C.-W. Qiu, G. Chen, and Y.-F. Xiao, Synchronization and temporal nonreciprocity of optical microresonators via spontaneous symmetry breaking, *Advanced Photonics* **1**, 1 (2019).
- [19] M. F. Colombano, G. Arregui, N. E. Capuj, A. Pitanti, J. Maire, A. Griol, B. Garrido, A. Martínez, C. M. Sotomayor-Torres, and D. Navarro-Urrios, Synchronization of Optomechanical Nanobeams by Mechanical Interaction, *Physical Review Letters* **123**, 17402 (2019).
- [20] M. Bagheri, M. Poot, L. Fan, F. Marquardt, and H. X. Tang, Photonic cavity synchronization of nanomechanical oscillators, *Physical Review Letters* 10.1103/PhysRevLett.111.213902 (2013).
- [21] X. Zhou, C. Zhao, D. Xiao, J. Sun, G. Sobrevela, D. D. Gerrard, Y. Chen, I. Flader, T. W. Kenny, X. Wu, and A. A. Seshia, Dynamic modulation of modal coupling in microelectromechanical gyroscopic ring resonators, *Nature Communications* **10**, 10.1038/s41467-019-12796-0 (2019).
- [22] R. Huan, D. Pu, X. Wang, and X. Wei, Effects of phase delay on synchronization in a nonlinear micro-mechanical oscillator, *Applied Physics Letters* **114**, 10.1063/1.5090977 (2019).
- [23] A. Ganesan and A. Seshia, Resonance tracking in a micro-mechanical device using phononic frequency combs, *Scientific Reports* **9**, 1 (2019).

- [24] U. Parlitz, L. Junge, and L. Kocarev, Subharmonic entrainment of unstable period orbits and generalized synchronization, *Physical Review Letters* **79**, 3158 (1997).
- 585 [25] C. Xu, S. Boccaletti, Z. Zheng, and S. Guan, Universal phase transitions to synchronization in Kuramoto-like models with heterogeneous coupling, *New Journal of Physics* **21**, 113018 (2019).
- [26] A. Cabot, F. Galve, and R. Zambrini, Dynamical and quantum effects of collective dissipation in optomechanical systems, *New Journal of Physics* **19**, 10.1088/1367-2630/aa8b9c (2017).
- 590 [27] M. H. Matheny, J. Emenheiser, W. Fon, A. Chapman, A. Salova, M. Rohden, J. Li, M. H. de Badyn, M. Pósfai, L. Duenas-Osorio, M. Mesbahi, J. P. Crutchfield, M. C. Cross, R. M. D'Souza, and M. L. Roukes, Exotic states in a simple network of nanoelectromechanical oscillators, *Science* **363**, 10.1126/science.aav7932 (2019).
- 595 [28] C. Sanavio, V. Peano, and A. Xuereb, Nonreciprocal topological phononics in optomechanical arrays, *Physical Review B* **101**, 1 (2020).
- 600 [29] S. Raeisi and F. Marquardt, Quench dynamics in one-dimensional optomechanical arrays, *Physical Review A* **101**, 23814 (2020).
- [30] S. Walter, A. Nunnenkamp, and C. Bruder, Quantum Synchronization of a Driven Self-Sustained Oscillator, *Physical Review Letters* 10.1103/PhysRevLett.112.094102 (2014).
- 605 [31] N. Lörch, E. Amitai, A. Nunnenkamp, and C. Bruder, Genuine Quantum Signatures in Synchronization of Anharmonic Self-Oscillators, *Physical Review Letters* **117**, 1 (2016).
- 610 [32] N. Lörch, S. E. Nigg, A. Nunnenkamp, R. P. Tiwari, and C. Bruder, Quantum Synchronization Blockade: Energy Quantization Hinders Synchronization of Identical Oscillators, *Physical Review Letters* **118**, 1 (2017).
- 615 [33] G. J. Qiao, X. Y. Liu, H. D. Liu, C. F. Sun, and X. X. Yi, Quantum ϕ synchronization in a coupled optomechanical system with periodic modulation, *Physical Review A* **101**, 1 (2020).
- 620 [34] A. Roulet and C. Bruder, Synchronizing the Smallest Possible System, *Physical Review Letters* **121**, 53601 (2018).
- 625 [35] N. Es'haqi-Sani, G. Manzano, R. Zambrini, and R. Fazio, Synchronization along quantum trajectories, *Physical Review Research* **2**, 23101 (2020).
- [36] M. Kennedy, K. Krieg, and L. Chua, The devil's staircase: the electrical engineer's fractal, *IEEE Transactions on Circuits and Systems* **36**, 1113 (1989).
- 630 [37] B. VAN DER POL and J. VAN DER MARK, Frequency Demultiplication, *Nature* **120**, 363 (1927).
- [38] S. Urazhdin, P. Tabor, V. Tiberkevich, and A. Slavin, Fractional synchronization of spin-torque nanoo oscillators, *Physical Review Letters* **105**, 10.1103/PhysRevLett.105.104101 (2010).
- 635 [39] M. Tortarolo, B. Lacoste, J. Hem, C. Dieudonné, M. C. Cyrille, J. A. Katine, D. Mauri, A. Zeltser, L. D. Buda-Prejbeanu, and U. Ebels, Injection locking at $2f$ of spin torque oscillators under influence of thermal noise, *Scientific Reports* **8**, 1 (2018).
- 640 [40] P. S. Keatley, S. R. Sani, G. Hrkac, S. M. Mohseni, P. Dürrenfeld, J. Åkerman, and R. J. Hicken, Superharmonic injection locking of nanocontact spin-torque vortex oscillators, *Physical Review B* **94**, 1 (2016).
- 645 [41] M. J. Seitner, M. Abdi, A. Ridolfo, M. J. Hartmann, and E. M. Weig, Parametric Oscillation, Frequency Mixing, and Injection Locking of Strongly Coupled Nanomechanical Resonator Modes, *Physical Review Letters* **118**, 10.1103/PhysRevLett.118.254301 (2017).
- 650 [42] D. Pu, X. Wei, L. Xu, Z. Jiang, and R. Huan, Synchronization of electrically coupled micromechanical oscillators with a frequency ratio of 3:1, *Applied Physics Letters* **112**, 1 (2018).
- [43] P. Taheri-Tehrani, M. Defoort, and D. A. Horsley, Observation of the effect of fractional synchronization on amplitude and frequency stability in micromechanical oscillators, *Journal of Microelectromechanical Systems* **28**, 578 (2019).
- 655 [44] S. Hourri, D. Hatanaka, M. Asano, R. Ohta, and H. Yamaguchi, Limit cycles and bifurcations in a nonlinear MEMS resonator with a 1:3 internal resonance, *Applied Physics Letters* **114**, 10.1063/1.5085219 (2019).
- [45] X. Du, D. F. Wang, C. Xia, S. Isao, and R. Maeda, Internal Resonance Phenomena in Coupled Ductile Cantilevers with Triple Frequency Ratio-Part I: Experimental Observations, *IEEE Sensors Journal* **19**, 5475 (2019).
- 660 [46] S. E. Brown, G. Mozurkewich, and G. Grüner, Subharmonic Shapiro Steps and Devil's-Staircase Behavior in Driven Charge-Density-Wave Systems, *Phys. Rev. Lett.* **52**, 2277 (1984).
- [47] J. F. Martinez Avila and J. R. Rios Leite, Time delays in the synchronization of chaotic coupled lasers with feedback, *Optics Express* 10.1364/oe.17.021442 (2009).
- 665 [48] J. Simonet, M. Warden, and E. Brun, Locking and Arnold tongues in an infinite-dimensional system: The nuclear magnetic resonance laser with delayed feedback, *Physical Review E* 10.1103/PhysRevE.50.3383 (1994).
- [49] J. K. Jang, X. Ji, C. Joshi, Y. Okawachi, M. Lipson, and A. L. Gaeta, Observation of Arnold Tongues in Coupled Soliton Kerr Frequency Combs, *Physical Review Letters* 10.1103/PhysRevLett.123.153901 (2019).
- 670 [50] T. O. Rocheleau, R. Liu, J. N. Nilchi, T. L. Naing, and C. T. Nguyen, A micromechanical parametric oscillator for frequency division and phase noise reduction, in *Proceedings of the IEEE International Conference on Micro Electro Mechanical Systems (MEMS)* (2014).
- [51] A. Amann, M. P. Mortell, E. P. O'Reilly, M. Quinlan, and D. Rachinskii, Mechanism of synchronization in frequency dividers, *IEEE Transactions on Circuits and Systems I: Regular Papers* **56**, 190 (2009).
- 675 [52] M. P. Kennedy, H. Mo, and X. Dong, Experimental characterization of Arnold tongues in injection-locked CMOS LC frequency dividers with tail and direct injection, 2011 20th European Conference on Circuit Theory and Design, ECCTD 2011 , 484 (2011).
- [53] J. T. Hill, A. H. Safavi-Naeini, J. Chan, and O. Painter, Coherent optical wavelength conversion via cavity optomechanics, *Nature Communications* **3**, 10.1038/ncomms2201 (2012).
- 680 [54] J. Chan, T. P. M. Alegre, A. H. Safavi-Naeini, J. T. Hill, A. Krause, S. Gröblacher, M. Aspelmeyer, and O. Painter, Laser cooling of a nanomechanical oscillator into its quantum ground state, *Nature* **478**, 89 (2011).
- [55] Y. Kato, N. Yamamoto, and H. Nakao, Semiclassical phase reduction theory for quantum synchronization, *Physical Review Research* **1**, 1 (2019).
- 685 [56] G. Heinrich, M. Ludwig, J. Qian, B. Kubala, and F. Marquardt, Collective Dynamics in Optomechanical Arrays,

- Phys. Rev. Lett. **107**, 43603 (2011).
- [57] M. Hossein-Zadeh and K. J. Vahala, Observation of injection locking in an optomechanical rf oscillator, *Applied Physics Letters* **93**, 1 (2008).
- [58] H. Wang, Y. Dhayalan, and E. Buks, Devil's staircase in an optomechanical cavity, *Physical Review E* 10.1103/PhysRevE.93.023007 (2016).
- [59] E. Amitai, N. Lörch, A. Nunnenkamp, S. Walter, and C. Bruder, Synchronization of an optomechanical system to an external drive, *Physical Review A* **95**, 1 (2017).
- [60] G. j. Qiao, H. x. Gao, H. d. Liu, and X. X. Yi, Quantum synchronization of two mechanical oscillators in coupled optomechanical systems with Kerr nonlinearity, *Scientific Reports* **8**, 1 (2018).
- [61] D. Rugar and P. Grütter, Mechanical parametric amplification and thermomechanical noise squeezing, *Physical Review Letters* **67**, 699 (1991).
- [62] V. Zega, S. Nitzan, M. Li, C. H. Ahn, E. Ng, V. Hong, Y. Yang, T. Kenny, A. Corigliano, and D. A. Horsley, Predicting the closed-loop stability and oscillation amplitude of nonlinear parametrically amplified oscillators, *Applied Physics Letters* **106**, 10.1063/1.4922533 (2015).
- [63] G. A. Brawley, M. R. Vanner, P. E. Larsen, S. Schmid, A. Boisen, and W. P. Bowen, Nonlinear optomechanical measurement of mechanical motion, *Nature Communications* **7**, 1 (2016).
- [64] K. Pelka, V. Peano, and A. Xuereb, Chimera states in small optomechanical arrays, *Physical Review Research* **2**, 1 (2020).
- [65] M. Zhang, S. Shah, J. Cardenas, and M. Lipson, Synchronization and Phase Noise Reduction in Micromechanical Oscillator Arrays Coupled through Light, *Physical Review Letters* 10.1103/PhysRevLett.115.163902 (2015).
- [66] F. Marquardt, J. G. Harris, and S. M. Girvin, Dynamical multistability induced by radiation pressure in high-finesse micromechanical optical cavities, *Physical Review Letters* **96**, 1 (2006).
- [67] R. Adler, A Study of Locking Phenomena in Oscillators, *Proceedings of the IEEE* **61**, 1380 (1973).
- [68] M. Zhang, G. S. Wiederhecker, S. Manipatruni, A. Barnard, P. McEuen, and M. Lipson, Synchronization of micromechanical oscillators using light, *Physical Review Letters* 10.1103/PhysRevLett.109.233906 (2012).
- [69] S. Y. Shah, M. Zhang, R. Rand, and M. Lipson, Master-slave locking of optomechanical oscillators over a long distance, *Physical Review Letters* **114**, 10.1103/PhysRevLett.114.113602 (2015).
- [70] M. Zhang, G. Luiz, S. Shah, G. Wiederhecker, and M. Lipson, Eliminating anchor loss in optomechanical resonators using elastic wave interference, *Applied Physics Letters* **105**, 10.1063/1.4892417 (2014).
- [71] X. Luan, Y. Huang, Y. Li, J. F. McMillan, J. Zheng, S. W. Huang, P. C. Hsieh, T. Gu, D. Wang, A. Hati, D. A. Howe, G. Wen, M. Yu, G. Lo, D. L. Kwong, and C. W. Wong, An integrated low phase noise radiation-pressure-driven optomechanical oscillator chipset, *Scientific Reports* **4**, 1 (2014).
- [72] I. Kovacic, R. Rand, and S. M. Sah, Mathieu's equation and its generalizations: Overview of stability charts and their features, *Applied Mechanics Reviews* **70**, 10.1115/1.4039144 (2018).
- [73] K. Y. Fong, M. Poot, X. Han, and H. X. Tang, Phase noise of self-sustained optomechanical oscillators, *Physical Review A - Atomic, Molecular, and Optical Physics* **90**, 1 (2014).
- [74] C. Mathai, S. A. Bhawe, and S. Tallur, Modeling the colors of phase noise in optomechanical oscillators, *OSA Continuum* **2**, 2253 (2019).
- [75] X. Zhang, X. Zhou, B. Aliener, and A. S. Daryoush, A Study of Subharmonic Injection Locking for Local Oscillators, *IEEE Microwave and Guided Wave Letters* **2**, 97 (1992).
- [76] S. Verma, H. R. Rategh, and T. H. Lee, A unified model for injection-locked frequency dividers, *IEEE Journal of Solid-State Circuits* **38**, 1015 (2003).
- [77] S. Kalia, M. Elbadry, B. Sadhu, S. Patnaik, J. Qiu, and R. Harjani, A simple, unified phase noise model for injection-locked oscillators, in *Digest of Papers - IEEE Radio Frequency Integrated Circuits Symposium* (2011).
- [78] A. Slavin and V. Tiberkevich, Nonlinear auto-oscillator theory of microwave generation by spin-polarized current, *IEEE Transactions on Magnetics* **45**, 1875 (2009).
- [79] M. Pandey, R. H. Rand, and A. T. Zehnder, Frequency locking in a forced Mathieu-van der Pol-Duffing system, *Nonlinear Dynamics* **54**, 3 (2008).
- [80] Y. Bai, G. Venugopalan, K. Kuns, C. Wipf, A. Markowitz, A. R. Wade, Y. Chen, and R. X. Adhikari, Phase-sensitive optomechanical amplifier for quantum noise reduction in laser interferometers, *Phys. Rev. A* **102**, 23507 (2020).
- [81] N. N. Bogoliubov and Y. A. Mitropolsky, *Asymptotic Methods in the Theory of Non-linear Oscillations*, International monographs on advanced mathematics and physics (Hindustan Publishing Corporation, [stamped, 1961]).

Figures

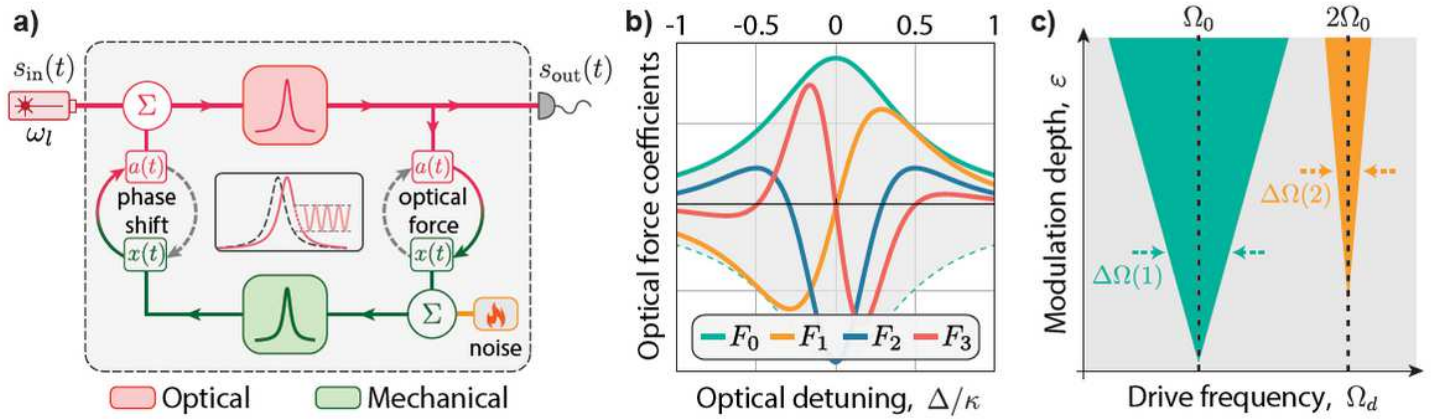


Figure 1

High-harmonic response of optomechanical oscillators. a) Optomechanical oscillator feedback diagram. The mechanical degree of freedom, $x(t)$, is initially in equilibrium with the thermal Brownian noise bath, but when a continuouswave laser excites the optical eld within the optical resonator, $a(t)$, the optical phase is imparted by the mechanical motion and transduced - via the optical resonance - to fluctuations on the optical energy. Due to radiation-pressure forces, the mechanical oscillator experiences a feedback (back-action) force that impacts its dynamics; b) Optical force components as function of the optical detuning $\Delta = \omega t - \omega_0$ shown in Eq. (1) (details in the Supplementary Information); c) Arnold tongues in the $\epsilon - \Omega_d$ space illustrating 1 : 1 and 2 : 1 entrainment.

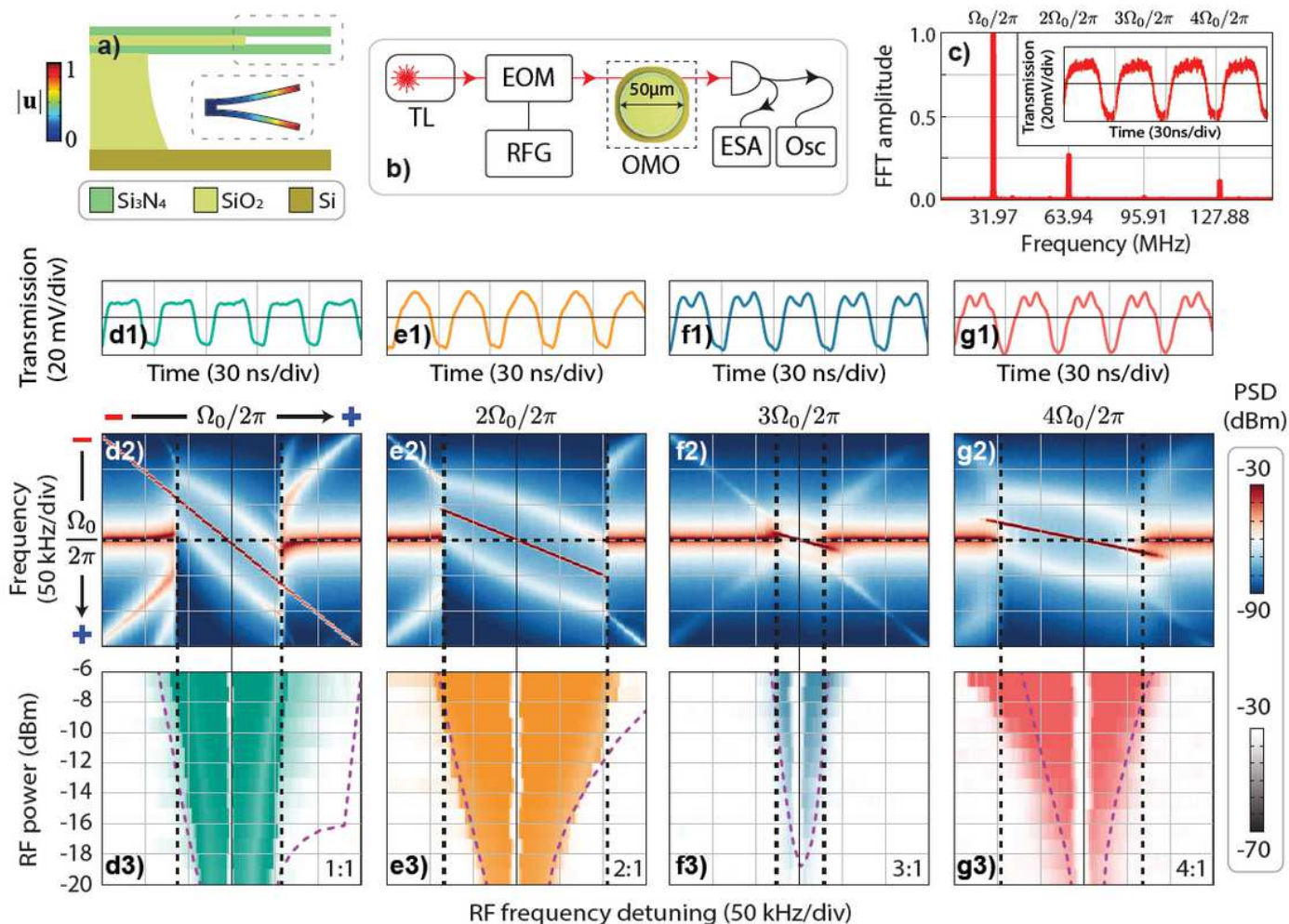


Figure 2

Experimental demonstration of multi-octave synchronization. a) Illustration of the silicon nitride dual-disk optomechanical cavity used in the experiment. The inset shows the simulated apping mechanical mode displacement profile $|u|$; b) Schematic of the experimental setup used; TL is the tunable laser source; EOM: electro-optic modulator; RFG: radiofrequency generator; ESA: electrical spectrum analyzer; Osc: oscilloscope; c) Magnitude of the fast-Fourier transform of the OMO output signal (inset); d1)-g1) Time-trace of the OMO output entrained at $p = 1$ (d1) until $p = 4$ (at g1). A RF injection power of -10 dBm ($\epsilon \approx 4\%$) was used; d2)-g2) RF spectrograms measured as the injection signal frequency is swept from lower to higher frequencies around each OMO harmonic, $p = 1$ (d2) until $p = 4$ (at g2), for an injection RF power of -10 dBm. The vertical RF frequency axis is always centered at the mechanical oscillation frequency $\Omega_0/2\pi$ and increases from top to bottom, as the symbols minus and plus suggests. The same is true for the horizontal axis, which increases from the left to the right; d3)-g3) Measured Arnold tongues corresponding to each harmonic, obtained by stacking horizontal linecuts along the dashed black line in data shown in d2)-g2). The purple curves are the simulated ATs and the colorscale of each plot matches the grayscale range shown in the right.

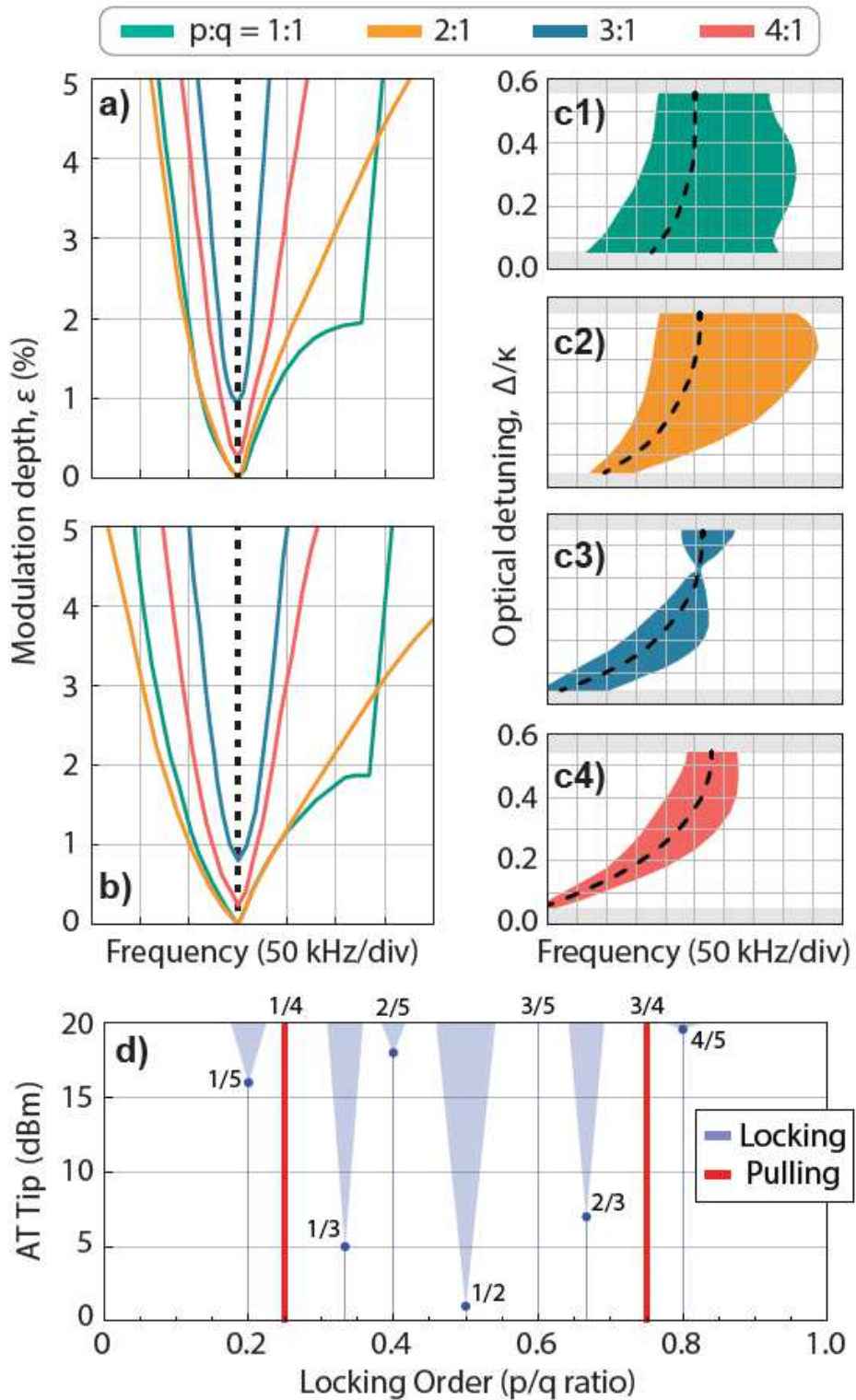


Figure 3

Numerical analysis and experimental observation of fractional synchronization. a) Arnold tongues boundaries simulated using the complete coupled optomechanical equations. The horizontal scale is the same used in experimental data of Fig. 2(d3-g3), revealing a good agreement; b) Same simulation done at a) but now considering only one parametric term in each simulation, i.e., the green ($1:1$) boundary was simulated considering $\varepsilon F_1 = \varepsilon F_2 = \varepsilon F_3 = 0$ but $\varepsilon F_0 \neq 0$ (details in the Supplementary Information). The

yellow (2 : 1) boundary has only the term $\epsilon F_1 \neq 0$, the blue (3 : 1) has $\epsilon F_2 \neq 0$ and the red (4 : 1) has $\epsilon F_3 \neq 0$; c1)-c4) Impact of optical detuning Δ in the ATs, showing their tunability and the possibility of a vanishing $p = 3$ tongue at $\Delta \approx 0.43\pi$ for the parameters used. These maps were simulated using $\epsilon = 5\%$ and the black-dashed line is the mechanical oscillation frequency, which increases with Δ because of the optical spring effect; d) Measured fractional synchronization threshold to observe a finite-width AT. The red-lines indicate the locking orders that did not synchronize and only frequency pulling was observed. The Arnold tongues shown are illustrations (see Supplementary Information for actual data).

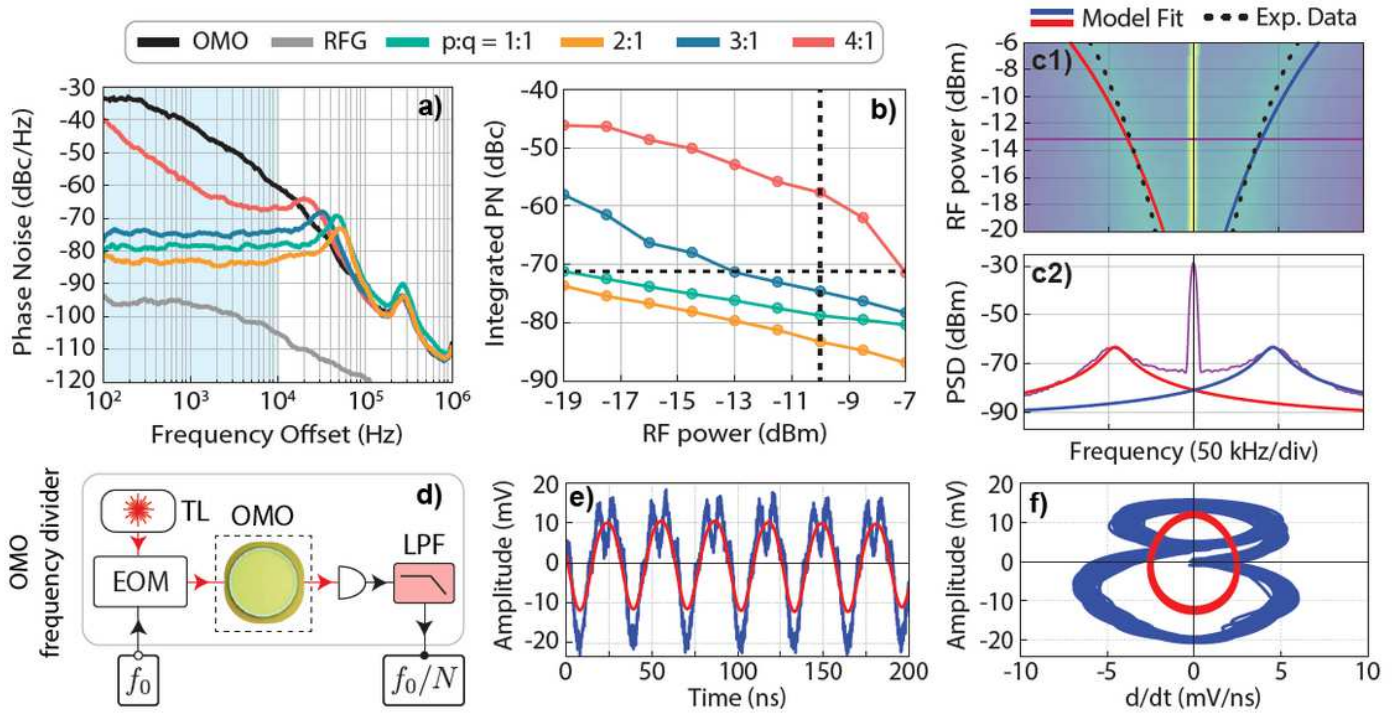


Figure 4

Phase-noise reduction and frequency division operation. a) Measured one-sided phase noise spectral density for the free-running (black), injection-locked (colored) and RF injection signal (gray); b) Integrated phase noise (from 100 Hz to 10 kHz, which is the light blue region of a)) for the injection locked OMO; color-code is shown in top bar; c1) Comparison between experimental data sidebands and the semi-analytical model. The colormap is the experimental PSD centered at $\Omega_0/2\pi$ showing the sidebands for reference; c2) Experimental power spectral density (PSD) in purple for a RF power of -13 dBm, which is the same horizontal purple linecut at c1), showing the agreement between semi-analytical model and experimental data for these sidebands, for both frequency and linewidth; d) Schematic of the optomechanical frequency divider; e) Optomechanical frequency division showing the raw and low-pass filtered OMO output under (4 : 1) injection with -10 dBm RF power; f) Phase-space plot of the time-domain signals shown in e).

Supplementary Files

This is a list of supplementary files associated with this preprint. Click to download.

- [Supplementary.pdf](#)